

# Discovery of a non-Hermitian phase transition in a bulk condensed-matter system

Jingwen Li,<sup>1</sup> Michael Turaev,<sup>2</sup> Masakazu Matsubara,<sup>3,4,5</sup> Kristin Kliemt,<sup>6</sup>  
Cornelius Krellner,<sup>6</sup> Shovon Pal,<sup>7</sup> Manfred Fiebig,<sup>1,\*</sup> and Johann Kroha<sup>2,8,†</sup>

<sup>1</sup>Department of Materials, ETH Zurich, Vladimir-Prelog-Weg 4, 8093 Zurich, Switzerland

<sup>2</sup>Physikalisches Institut and Bethe Center for Theoretical Physics, University of Bonn, 53115 Bonn, Germany

<sup>3</sup>Department of Physics, Tohoku University, Sendai 980-8578, Japan

<sup>4</sup>Center for Science and Innovation in Spintronics, Tohoku University, Sendai 980-8577, Japan

<sup>5</sup>PRESTO, Japan Science and Technology Agency (JST), Kawaguchi 332-0012, Japan

<sup>6</sup>Physikalisches Institut, Goethe-Universität Frankfurt, 60438 Frankfurt, Germany

<sup>7</sup>School of Physical Sciences, National Institute of Science Education and Research, An OCC of HBNI, Jatni, 752 050 Odisha, India

<sup>8</sup>School of Physics and Astronomy, University of St. Andrews,  
North Haugh, St. Andrews, KY16 9SS, United Kingdom

(Dated: December 23, 2024)

Phase transitions are fundamental in nature. A small parameter change near a critical point leads to a qualitative change in system properties. Across a regular phase transition, the system remains in thermal equilibrium and, therefore, experiences a change of static properties, like the emergence of a magnetisation upon cooling a ferromagnet below the Curie temperature. When driving a system far from equilibrium, novel, otherwise inaccessible quantum states of matter may arise. Such states are typically non-Hermitian, that is, their dynamics break time-reversal symmetry, a basic law of equilibrium physics. Phase transitions in non-Hermitian systems are of fundamentally new nature in that the *dynamical behaviour* rather than static properties may undergo a qualitative change at a critical, here called exceptional point. Here we experimentally realize a non-Hermitian phase transition in a bulk condensed-matter system. Optical excitation creates charge carriers in the ferromagnetic semiconductor EuO. In a temperature-dependent interplay with the Hermitian transition to ferromagnetic order, a non-Hermitian change of the relaxation dynamics occurs, manifesting in our time-resolved reflection data as a transition from bi-exponential real to single-exponential complex decay. Our theory models this behavior and predicts non-Hermitian phase transitions for a large class of condensed-matter systems, where they may be exploited to sensitively control bulk-dynamic properties.

Both in basic research and application, phase transitions are usually considered under the aspect of a lasting change of ground-state properties, where the system undergoing a phase transition remains in thermodynamic equilibrium at all times. In a good approximation, this even holds when the phase transition occurs on very short timescales, for example, when pulsed lasers are used for controlling magnetically ordered states. The associated field of ultrafast magnetisation dynamics was kick-started in 1996<sup>1</sup> and has flourished ever since. The photo-excitation is used either to drive phase transitions in an all-optical way<sup>2-5</sup> or to separate the various interaction processes determining the

ground state of a material via their respective relaxation times<sup>6-9</sup>.

Even though by now the field has reached the femtosecond regime, ultrafast techniques are essentially still concerned with the manipulation of magnetic phases defined with respect to equilibrium physics. Driving a system truly away from thermodynamic equilibrium could, therefore, offer unique insights into dynamical processes in materials in that qualitatively new states of matter may be created that are characterised by their dynamics rather than their ground-state properties and cannot be realised otherwise. This leads us to the subject of non-Hermitian phase transitions (NHPTs)<sup>10</sup>. In contrast to equilibrium systems, which are invariant with respect to the reversal of time as a fundamental law of nature, excitation and dissipation break time-reversal symmetry. This usually manifests in an asymmetry between the drive and loss terms. The matrix connecting the response of a system's properties to the driving fields becomes non-Hermitian, its eigenvalues thus in general complex, and its eigenvectors non-orthogonal. While at an equilibrium phase transition, the free energies of two static phases (at zero temperature, the energies of two quantum states) become equal, a NHPT occurs in physical systems when two real eigenvalues of a non-equilibrium response matrix  $\chi$  become equal and change into a single complex-conjugate pair. Formally, this can be expressed by eigenvalues  $\gamma_{1,2}$  of the form  $\gamma_{1,2} = x \pm \sqrt{y}$ , where  $y$  changes its sign from "+" to "-" at the exceptional point (EP)<sup>11</sup>. In consequence, the corresponding eigenvectors coalesce, which means physically that the two modes of the system dynamics collapse into a single one. This is accompanied by a qualitative change of the dynamical behaviour with enhanced sensitivity to a variation of external parameters near the EP. Therefore, a NHPT generally represents a phase transition in the *dynamics* of a system rather than in its ground-state properties as in the Hermitian case. It is this exotic dynamical behavior that has generated the immense fundamental and possibly also application-wise interest in NHPTs. Most of its studies are theoretical, while experimental realisations have focused on nanoscopic<sup>12</sup>, nanophotonic<sup>13</sup>, ultracold-atomic-gas<sup>14,15</sup>, or photon-condensate systems<sup>16</sup>. The possibility of a NHPT in a solid condensed-matter system has not even been dis-

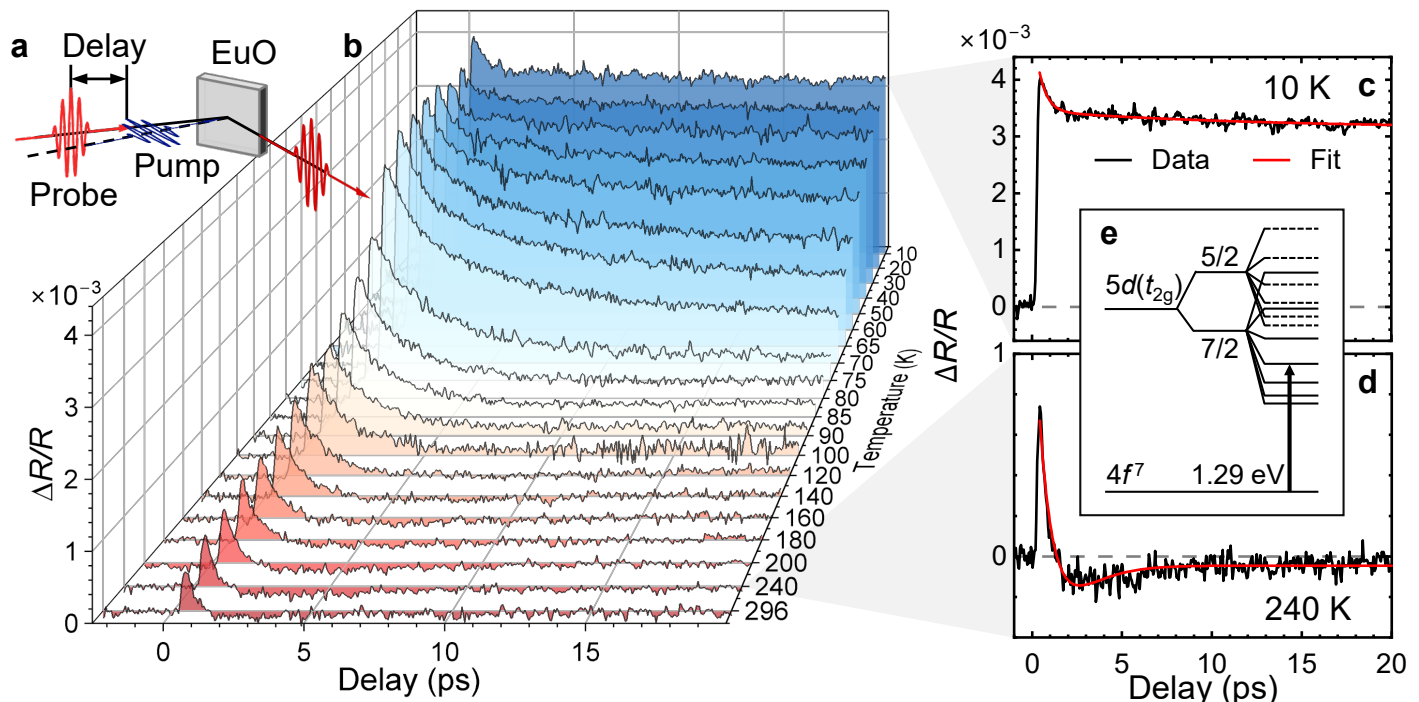


Figure 1. **Photoinduced reflectivity change in EuO.** **a**, A 120-fs laser pulse (blue) with an energy density of  $100 \mu\text{J}/\text{cm}^2$  and a photon energy of 1.55 eV drives the system out of equilibrium and excites electrons from the Eu  $4f$  shell to the Eu  $5d(t_{2g})$  orbitals. Time-delayed probe pulses (red) of 1.31 eV induce resonant recombination of  $5d(t_{2g})$  electrons with holes in the Eu  $4f$  shell; see (e). The photons emitted by this recombination contribute to the reflectivity change. **b**, Relative change of reflectivity with respect to the non-pumped system as a function of delay time for temperatures from 10 to 296 K. The NHPT occurs when the relaxation dynamics changes from **c**, bi-exponential positive to **d**, sign-changing; see text. **e**, Electronic level scheme around the semiconductor gap of EuO<sup>24–26</sup>. Splittings of the bare conduction-electron states (left) are caused by spin-orbit interaction (center) and crystal-electric-field coupling (right).

cussed because it was considered unfeasible to establish the required extreme off-equilibrium state in bulk systems.

Here, we report on the observation of a NHPT in the bulk ferromagnetic semiconductor europium monoxide (EuO) after optical excitation of electrons from the  $4f$  valence to the  $5d$  conduction band of the Eu ions. Time-resolved pump-probe measurements of the linear reflectivity reveal the characteristic “smoking-gun” change of the ensuing relaxation dynamics from two real to a single complex-conjugate decay rate. The EP of this transition is observed at 84 K and thus distinctly higher than the Curie temperature  $T_C$  of the Hermitian phase transition to ferromagnetic order at 69 K. We show that in a many-body system, a Hermitian and a NHPT may be linked to each other as originating from the same microscopic coupling mechanism, albeit representing very different physical phenomena occurring at different critical temperatures. We finally propose that NHPTs should be permitted for a large class of condensed-matter systems, where they may be exploited to sensitively control bulk-dynamic properties.

EuO exhibits a rocksalt structure and has a large semiconductor gap of 1.2 eV. The ferromagnetic order of the Eu  $4f^7$  ions is mediated by virtual magnetic polarons involving charge-carrier fluctuations in the spatially extended Eu  $5d(t_{2g})$  orbitals that interconnect the tightly bound Eu  $4f^7$  magnetic moments<sup>17</sup>. Doping charge car-

riers into the  $5d(t_{2g})$  conduction orbitals by chemically substituting Eu with Gd atoms enhances  $T_C$  even further<sup>18,19</sup> via the conduction-electron-mediated Ruderman-Kittel-Kasuya-Yosida (RKKY) interaction<sup>20</sup>. Alternatively,  $4f^7 \rightarrow 5d(t_{2g})$  photodoping leads to a transient strengthening of the magnetic order<sup>21</sup>. Both effects underpin the importance of the magnetic coupling  $J_{df}$  between the  $4f$  local moments and  $5d$  conduction spins in EuO, which will become important below. The ferromagnetic transition is accompanied by a pronounced Stoner band splitting, which shifts spectral weight below the Fermi energy and, thus, makes the material metallic with nearly completely spin-polarised electrons at low temperature<sup>22,23</sup>.

We use EuO single crystals grown by the gradient cooling technique with a Bridgman setup<sup>27</sup>. Crystals are cut to produce a [100]-oriented surface, lapped to a thickness of  $280 \mu\text{m}$  on SiC films, and polished with  $\text{Al}_2\text{O}_3$  films in ethanol. In a pump-probe experiment sketched in Fig. 1a, a 120-fs pump pulse of 1.55 eV, generated by an amplified Ti: sapphire laser system, promotes electrons from the Eu  $4f$  valence to the  $5d(t_{2g})$  conduction band. Note that the total spin  $S = 7/2$  is conserved in this transition. We then record the change in reflectivity,  $\Delta R(t)/R$ , with respect to the non-pumped system after a delay time  $t$ . For this we use 120-fs laser pulses at 1.31 eV, which are emitted by a

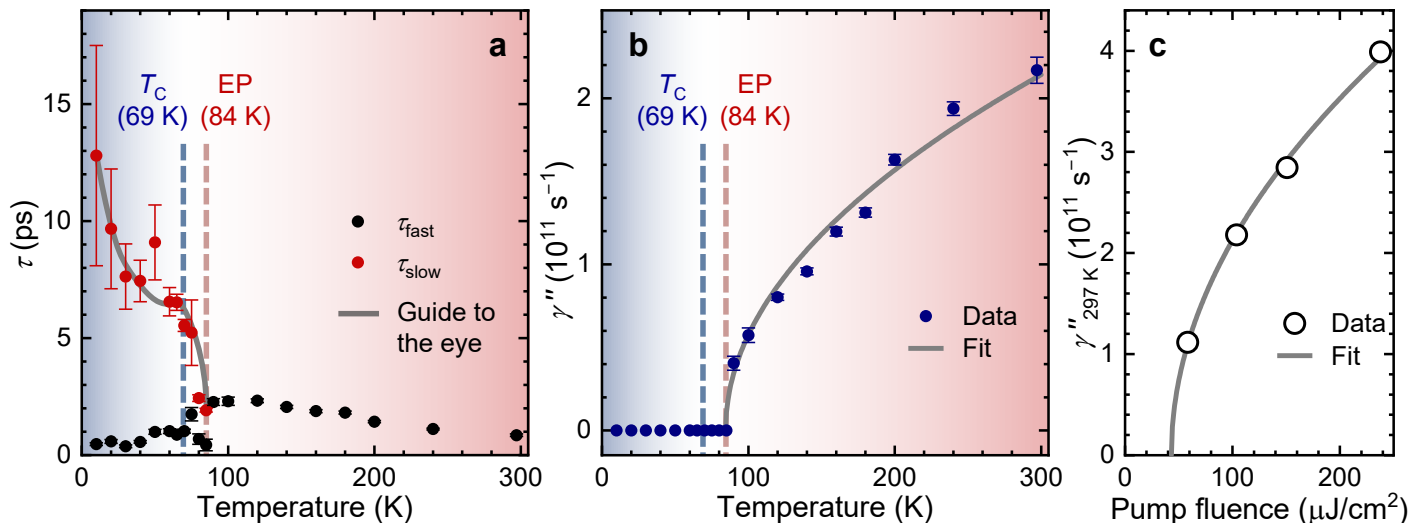


Figure 2. **Hallmarks of a non-Hermitian phase transition.** **a**, The bi-exponential relaxation times  $\tau_{\text{fast}}$ ,  $\tau_{\text{slow}}$  and **b**, the imaginary part  $\gamma''$  of the relaxation rate  $\gamma$  are shown as a function of temperature, extracted from the time traces of Fig. 1b. The appearance of a non-zero value  $\gamma''$  at the critical temperature of  $T^* \approx 84 \text{ K}$  marks the exceptional point (EP). Note the cusp-like feature in  $\tau_{\text{fast}}$  and  $\tau_{\text{slow}}$  at the ferromagnetic ordering temperature  $T_C = 69 \text{ K}$ . **c**, Relaxation parameter  $\gamma''$  as a function of pump fluence  $P$ . The fitted scaling behaviors  $\gamma'' \sim \sqrt{T - T^*}$  above the EP for fixed pump fluence and  $\gamma'' \sim \sqrt{P - P^*}$  at fixed temperature are in excellent agreement with theory and pose unambiguous signatures of a NHPT (see text and Fig. 4). At the temperature of  $T = 297 \text{ K}$ , the threshold pump fluence for the onset of complex relaxation is  $P^* \approx 42 \mu\text{J}/\text{cm}^2$ .

downstream optical parametric amplifier and incident under an angle of  $45^\circ$ . These pulses probe the dipole-allowed, spin-conserving electronic  $\text{Eu } 5d(t_{2g}) \rightarrow 4f$  transition at 1.29 eV resonantly, see the level scheme in Fig. 1e. Figure 1b shows the corresponding reflectivity time traces after optical pumping between 10 K and 296 K.

Across this temperature range, the relaxation behaviour exhibits a drastic qualitative change. In all cases, we observe an initial increase of the reflectivity that peaks within the duration of the laser pulse. Towards low temperature, the ensuing relaxation exhibits a rapid, continuous decay of the reflectivity change on a time scale of about 1 ps, followed by a much slower, second relaxation (Fig. 1c). In the ferromagnetic phase, the reflectivity change  $\Delta R/R$  settles for long times to a positive value, indicating that the optically induced conduction-band population is energetically stabilised by the aforementioned Stoner shift<sup>22,23</sup> of the majority conduction band below the Fermi energy at least throughout our observed time range of 20 ps. Towards high temperature, however, the initial reflectivity peak is followed by a single rapid decay reaching a negative amplitude before approaching the original value at  $\Delta R = 0$  (Fig. 1d). For the pump fluence of  $100 \mu\text{J}/\text{cm}^2$  used in the experiment, the transition from the all-positive to the partly negative evolution of  $\Delta R/R$  occurs in the paramagnetic phase, at a threshold temperature  $T^* = (84 \pm 5) \text{ K} > T_C$  (see Supplementary Information).

We point out that none of the phenomena known to possibly cause a negative dynamic response can explain the behavior of our present system in Fig. 1d. Among the more than 10 effects we examined are, for example, oscillations induced by coupling to coherent lattice vibrations<sup>28</sup>. In

the rock-salt structure of  $\text{EuO}$ , however, the relevant optical phonons are at a much higher frequency<sup>29</sup> than the one corresponding to the slow  $\sim 10 \text{ ps}$  dynamics observed in our experiments. A negative dynamical response may generally also be caused by Auger recombination<sup>30,31</sup>. In a metal or doped semiconductor, a photoexcited electron could recombine with a hole in a radiation-less way by exciting another electron to higher energy, thus reducing the number of carriers contributing to the reflectivity. However, in insulating  $\text{EuO}$  above 69 K, Auger recombination would be of second order in the carrier density and, thus, proportional to the square of the pump fluence, in contrast to the experimental observations (see below). In addition, exponential relaxation with a negative amplitude that could describe the Auger photocarrier depletion<sup>31</sup> fails to fit our experimental results, see Supplementary Information. We can furthermore exclude band-filling effects in semiconductors<sup>33-36</sup>, which occur at higher fluence, and we do not further discuss phenomena occurring on different time scales<sup>37</sup>, in different frequency ranges (THz)<sup>32,38</sup>, or in different material phases like superconductivity<sup>39</sup>. In particular, none of these effects can explain (i) a critical temperature  $T^*$  beyond which the negative response occurs, and (ii) the peculiar temperature and pump-fluence dependencies of the relaxation rates shown below.

Having thus excluded known physical origins for the measured pump-induced reflectivity decrease, we now show that our observed response exhibits, in fact, the unique signature of a NHPT. For further analysis, we extract the relaxation rates  $\gamma_1$ ,  $\gamma_2$  at  $T < T^*$  by a bi-exponential fit

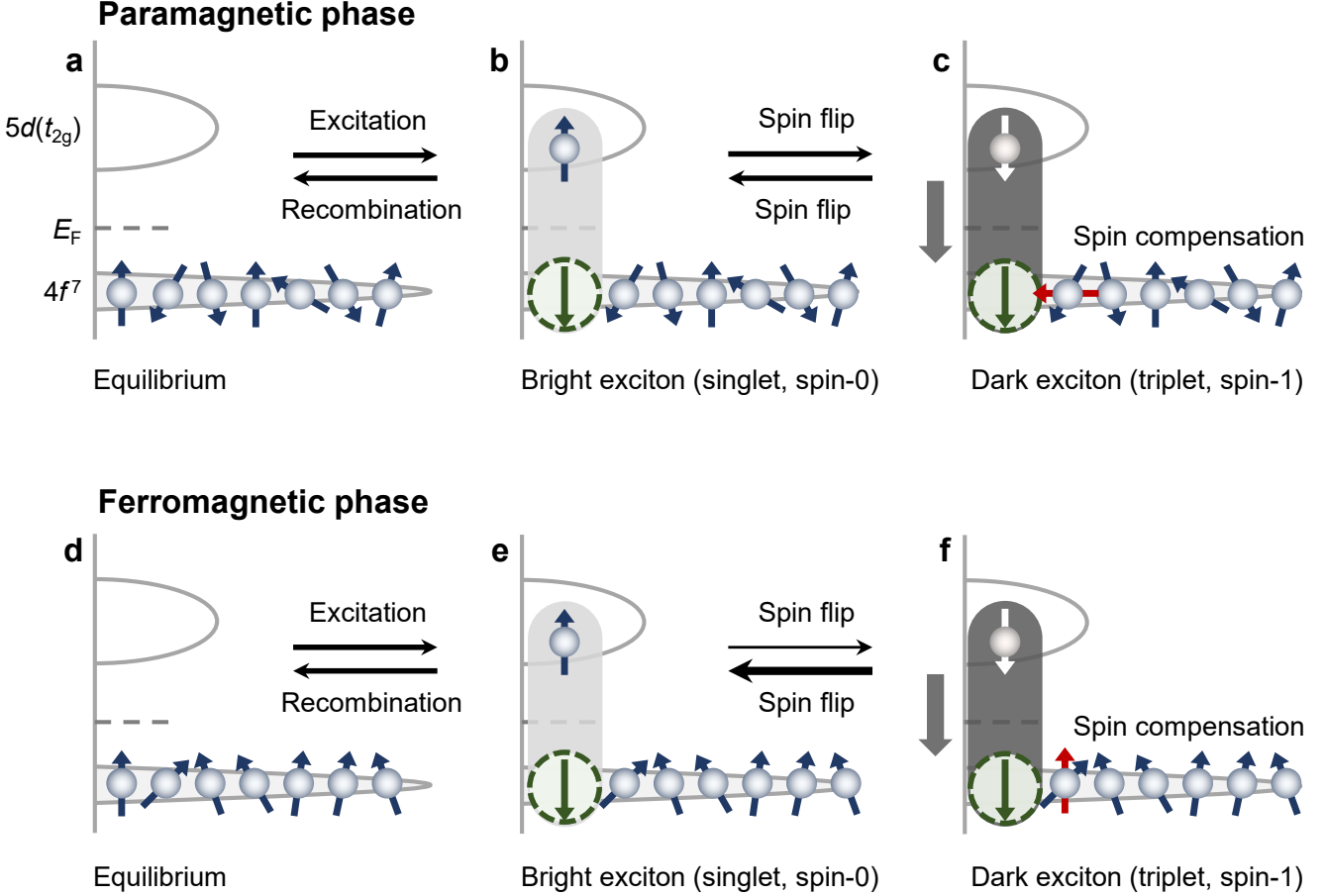


Figure 3. **Schematic of the coupled spin-charge dynamics in EuO.** **a-c.** Paramagnetic phase. **a,** The electronic structure of EuO is comprised of a Eu  $4f^7$  valence band and a  $5d(t_{2g})$  conduction band, with the Fermi level  $E_F$  in the gap of 1.2 eV. **b,** Photoexcitation of electrons at 1.55 eV into the Eu  $5d(t_{2g})$  orbitals generates bright excitons which can recombine by the emission of a photon at 1.31 eV. This is recorded in the experiments as the positive reflectivity change  $\Delta R/R$ . **c,** Before recombination, a bright exciton (spin 0) can be transformed into a dark exciton (spin 1) by flipping the electron spin by interaction with a Eu  $4f$  ( $7/2$ ) magnetic moment. The total spin is conserved by the  $4f$  magnetic moments changing their orientation accordingly (blue-to-red orientation). The spin-1 excitons cannot directly recombine reduces the density of photoemitting charge carriers and thus leads to the negative contribution to  $\Delta R/R$ . **d-f,** Ferromagnetic phase. The preferred orientation of the  $4f$  spins induces an asymmetry between bright-to-dark and dark-to bright exciton transitions (spin-flip arrows of different thickness). Its onset leads to a cusp in the relaxation times at the Curie temperature that is visible in Figs. 2a and 4a.

according to

$$\frac{\Delta R(t)}{R} = C_1 e^{-\gamma_1 t} + C_2 e^{-\gamma_2 t}, \quad (1)$$

with  $C_{1,2} > 0$  and  $\gamma_{1,2}$  and  $C_{1,2}$  as real values, to the experimental data. For describing the negative response at  $T > T^*$ , there are two options. First, we can assume that either  $C_1$  or  $C_2$  become negative. As we show in the supplement, this leads to large errors and an inconsistent temperature dependence of the fit parameters. Second, we allow for complex relaxation rates and set  $\gamma_{1,2} = \gamma' \pm i\gamma''$  and  $C_{1,2} = C_0 e^{\pm i\varphi_0}$ , with real values  $\gamma'$ ,  $\gamma''$ ,  $C_0$ , and  $\varphi_0$ , so that real values for  $\Delta R(t)/R$  are retained. The results for the relaxation time(s)  $\tau = \text{Re}(\gamma)^{-1}$  and the relaxation parameter  $\gamma'' = \text{Im}(\gamma)$  are shown in Fig. 2. For  $T < T^*$

we observe bi-exponential relaxation with two relaxation times, while for  $T > T^*$  the dynamical behavior collapses to a single relaxation mode with positive and negative parts caused by the complex nature of the relaxation rate. This collapse at a specific temperature  $T^*$  bears a most striking resemblance to a system undergoing a NHPT. In particular, while, as done above, several physical processes may be evaluated as cause of a negative signal like in Fig. 1d, *none of these processes aside from the NHPT* can explain the very specific square-root dependencies of the relaxation parameter on temperature and pump fluence  $P$  shown in Fig. 2, see Supplementary Information.

In the following, we present a theoretical model which explains the occurrence of a NHPT in EuO in a natural way and describes all the temperature- and fluence-dependent

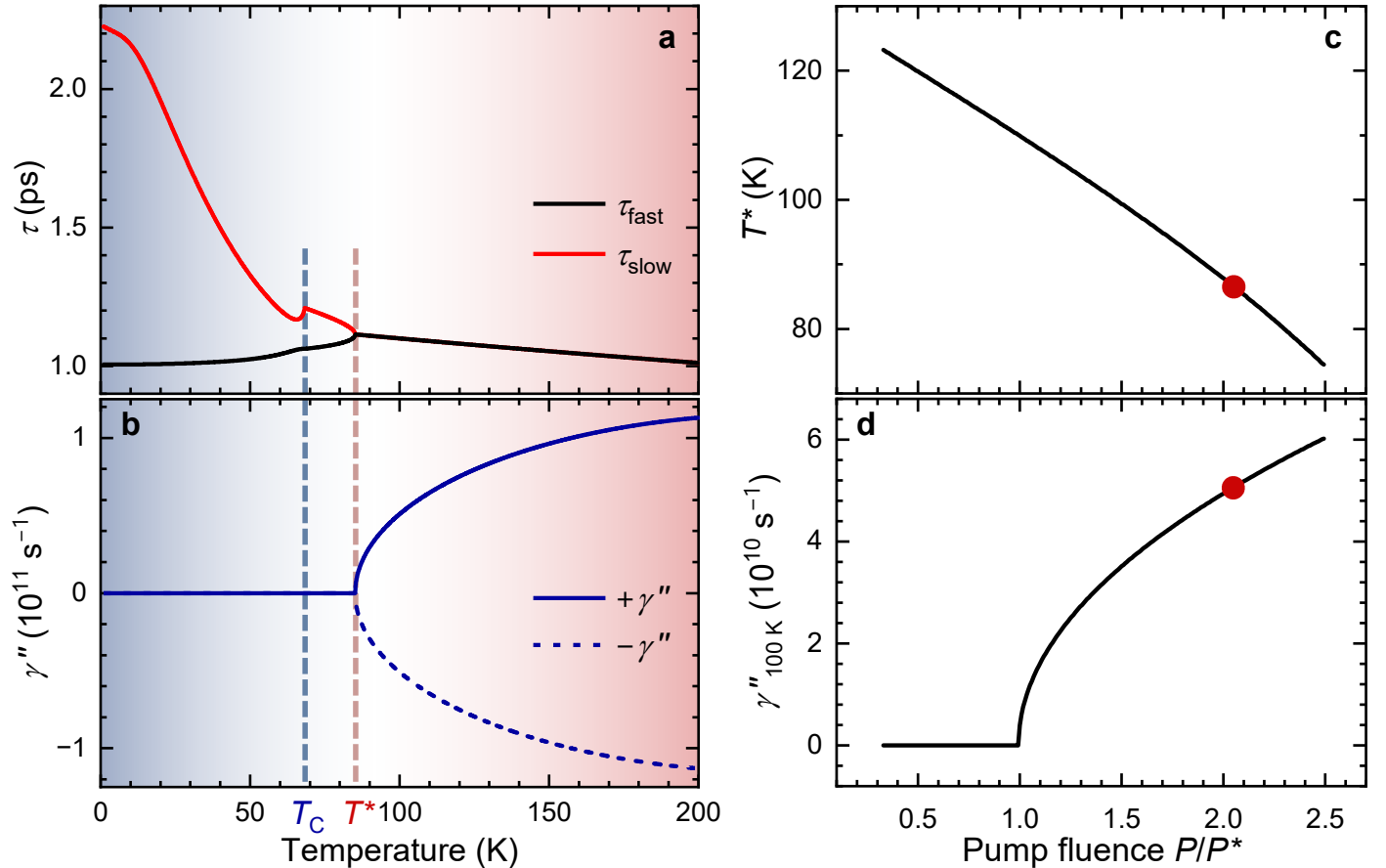


Figure 4. **Theoretical results.** **a, b**, Relaxation times  $\tau_{\text{fast}}$ ,  $\tau_{\text{slow}}$  as well as the imaginary part  $\gamma''$  of the relaxation rate  $\gamma$  are shown as a function of temperature, exhibiting an exceptional point at  $T^*$ . Parameters used for the calculations: see Supplementary Information, Table 1. The striking qualitative agreement with the experimental observations (Fig. 2), including the cusp at  $T_C$ , strongly supports our model and the presence of a NHPT. **c**, Dependence of the EP at  $T^*$  on the pump fluence  $P$  as calculated from the Lindblad dynamical equations, see Methods and Supplementary Information. **d**, The dependence of  $\gamma''$  on  $P^*$ , here calculated at 100 K, scales as  $\sqrt{P - P^*}$  beyond the critical pump fluence  $P^*$ , again in agreement with the experimental observation in Fig. 2. The red dots in **c** and **d** indicate the pump fluence used for the calculations in **a**, **b**.

features on the same footing, including the cusp visible in Fig. 2a at the Curie temperature  $T_C$ . To that end, we first identify the dynamical variables active in our material. The change of reflectivity after optical excitation is proportional to the density of photoexcited charge carriers in the conduction band, which recombine with holes in the valence band by the emission of a photon. Excitations of this type, Wannier excitons, have long been known to exist in  $\text{EuO}^{40}$ . Since the reflectivity exhibits bi-exponential relaxation after optical pumping at low temperature, there must be two types of electronic excitations. These are “bright” (optically excitable) and “dark” (non-radiatively decaying) excitons, both formed as a bound state of a  $5d(t_{2g})$  electron and a  $4f$  hole in the valence band. Furthermore, it is known that the conduction-electron spin couples strongly to the  $\text{Eu } 4f^7$  local moments via a Heisenberg exchange coupling  $J_{df}$  (see introductory remarks on  $\text{EuO}$  above).

Putting this together, an ultrashort optical laser pulse excites electrons across the semiconductor gap of 1.2 eV without spin flip, thus creating bright excitons which can

recombine by the emission of a photon and induce the measured reflectivity change (Fig. 3a,b; d,e). Alternatively, a conduction electron can flip its spin with a  $\text{Eu } 4f$  local moment via the coupling  $J_{df}$ , thus transforming a bright spin-0 exciton into a dark spin-1 exciton and vice versa (Fig. 3c,f). The spin-1 exciton cannot recombine by emitting a photon via the spin-conserving dipole decay, thus reducing the reflectivity below its equilibrium value. During the bright-dark exciton transformation, the orientation of the randomly oriented  $\text{Eu } 4f$  moments is altered as well. Because of the different energies of spin-0 and spin-1 excitons (see Fig. 1e), the bright-dark transformation processes are dissipative and thus energy non-conserving. The energy difference is absorbed or provided by a thermal bath of phonons at the cryostat temperature  $T$ . This induces an asymmetry between the bright-dark and the dark-bright transformation amplitudes,  $\Gamma^+$ ,  $\Gamma^-$ , which breaks time-reversal symmetry and makes these amplitudes temperature-dependent, as derived formally by the Lindblad formalism<sup>41</sup>.

In the paramagnetic phase, this leads to a set of two

coupled rate equations for the densities of bright and dark excitons,  $n_{b,d}(t)$ . The equations are parameterised by a real-valued, non-symmetric  $2 \times 2$  matrix  $\chi(T)$ , see Methods and Supplementary Information. Its eigenvalues are the relaxation rates  $\gamma_1$  and  $\gamma_2$  of the bright-dark-exciton-coupled system and are the solutions of a quadratic equation of the form

$$\gamma_{1,2} = \left[ \gamma_b + \gamma_d \pm \sqrt{(\gamma_b - \gamma_d)^2 - 4\omega_0^2} \right] / 2, \quad (2)$$

where  $\gamma_b$ ,  $\gamma_d$  are the diagonal elements of  $\chi$ , i.e., the bright/dark exciton decay rates without mutual coupling, and  $\omega_0^2$  is the modulus of the product of the off-diagonal elements of  $\chi$ . That is,  $\omega_0$  is the natural frequency of the bright-dark-exciton-coupled system, if there were no dissipation. Figures 4a and 4b show the relaxation times  $\tau_{\text{fast}}$ ,  $\tau_{\text{slow}}$  and the relaxation parameter  $\gamma''$  as the inverse real parts and as the imaginary part of these eigenvalues, respectively, whose temperature dependence is inherited from the transition amplitudes  $\Gamma^\pm(T)$ . The EP is reached when the argument of the square root in Eq. (2), crosses zero at the critical temperature  $T^*$  of the NHPT. As the possibly most striking and unique feature associated with the NHPT, Eq. (2) predicts that the imaginary part of the relaxation rate behaves as  $\gamma'' \sim \sqrt{T - T^*}$  for  $T \geq T^*$ , see Fig. 4b. This is because the argument of the square root crosses zero linearly at the critical values. The fact that the experiment shows precisely this behaviour (see Fig. 2b), which is not expected from any other physical phenomenon, is an unambiguous confirmation that optically pumped EuO exhibits a NHPT with the sample temperature as the control parameter.

In the ferromagnetic phase, the  $4f$  spin orientation acquires, in addition to the time-dependent variation, a non-zero, static equilibrium value, the magnetisation, which has the temperature dependence  $M(T) = M_0\sqrt{T_C - T}$ . This temperature dependence manifests in the relaxation times as a cusp visible in Fig. 4a near the Curie temperature  $T_C$ . A similar feature appears in the experimental data, Fig. 2a, at  $T_C = 69$  K, which lends additional support for the correctness of our model and, hence, for the existence of the NHPT. The ferromagnetic transition and the NHPT are closely related since they are caused by the same microscopic interaction, namely the spin coupling  $J_{df}$  between Eu  $4f$  moments and the electrons in the  $5d(t_{2g})$  orbitals. However, they represent fundamentally different physical phenomena generally occurring at different critical temperatures,  $T_C$  and  $T^*$ , respectively.

We furthermore note that the relaxation parameter  $\gamma''$  is not a fixed intrinsic material parameter but of dynamic origin, determined by the interplay of bright-dark exciton transformation and dissipation. The pump fluence  $P$  controls how far the system is driven into non-equilibrium and determines the initial, photoexcited exciton densities  $\bar{n}_b$ ,  $\bar{n}_d$ . Our model thus predicts that with increasing pump fluence the EP at  $T^*$  shifts towards lower values (Fig. 4c). At a given temperature, the imaginary part of the decay rate therefore scales as  $\gamma'' \sim \sqrt{P - P^*}$  across the NHPT at the critical pump fluence  $P^*$  (Fig. 4d). Again, this pre-

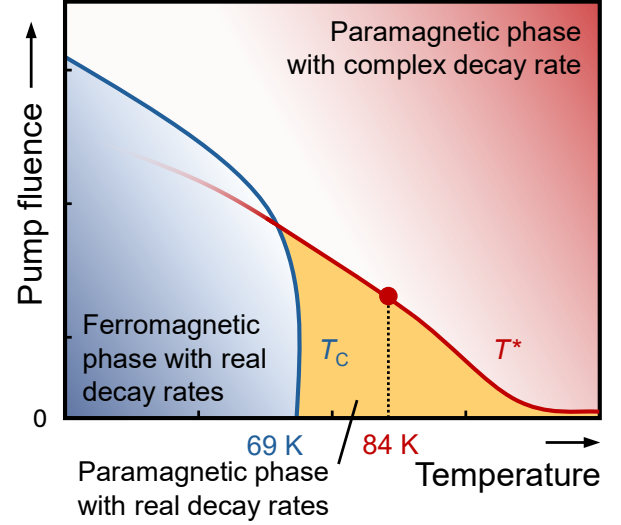


Figure 5. **Schematic phase diagram of the ferromagnetic and the non-Hermitian phase transitions in EuO.** Upon increasing the pump fluence, the conduction-electron-mediated ferromagnetic coupling between the Eu  $4f$  moments transiently increases<sup>21</sup> without significantly increasing the Curie temperature  $T_C$  on the picosecond time scale. For stronger pump fluence,  $T_C$  is reduced due to the increasing occurrence of inelastic processes. The decrease of  $T^*$  with the increase of  $P$  is derived from Fig. 4b. The red dot marks the temperature  $T^*$  where the NHPT was detected at the pump fluence used in the experiment. Note that it may be possible to tune  $T^*$  to coincide with  $T_C$ , thus creating a critical EP with altered critical fluctuations and enhanced sensitivity to external parameters.

diction is beautifully supported by our experiments; see Fig. 2c. This gives rise to the schematic phase diagram shown in Fig. 5.

To conclude, we have discovered a new dynamical state of matter in the exciton gas of a bulk solid-state material, europium oxide, which manifests itself by complex relaxation behavior detected in our optical pump-probe experiments. The non-equilibrium phase diagram of EuO encompasses both, a Hermitian phase transition to ferromagnetic order and, as reported here, a NHPT towards the new dynamical phase. Both transitions are mediated by the same magnetic coupling of Eu  $4f^7$  moments and  $5d(t_{2g})$  electrons, but represent separate phenomena occurring in general at different critical temperatures,  $T_C$  and  $T^*$ , respectively. We suggest that both critical temperatures in EuO may be tuned to coincide at a feasible pump fluence with characteristically altered critical fluctuations and enhanced sensitivity to parameter changes as a consequence<sup>42</sup>. This may be verified once we have found a way to realise the necessary laser pump fluence. The generality of our theoretical model suggests that similar non-Hermitian phase transitions can occur in a wide variety of materials that exhibit a two-component dynamics coupled by a third mode.

## METHODS

**Sample growth:** EuO single crystals were grown in a tungsten crucible enclosed in tantalum by combining high-purity  $\text{Eu}_2\text{O}_3$  (99.9%) and Eu (99.99%) in a ratio of 1:3 as starting constituents. The Eu excess was necessary to suppress the formation of  $\text{Eu}_3\text{O}_4$ . Crystal growth was accomplished by cooling the melt from 2280 to 1180 °C over five hours in a high-frequency “Arthur D. Little” furnace using a Bridgman setup. See Ref.<sup>27</sup> for details of the growth procedure. The obtained specimen had a volume of about 0.5 cm<sup>3</sup>. The excess Eu was found on top of the grown crystal and immediately formed Eu oxide ( $\text{Eu}_2\text{O}_3$ ) upon air contact. This  $\text{Eu}_2\text{O}_3$  layer was removed by polishing, and subsequent Laue diffractometry showed that the grown sample was one large EuO single crystal with minor misorientation caused by small-angle-grain-boundary formation. Magnetisation and specific-heat measurements confirmed that samples exhibit the corresponding physical properties known from the literature<sup>43</sup>. Before the optical measurements, all samples were hand-polished to get a fresh [100]-cut surface.

**Pump-probe experiments:** The samples were placed in a Janis SVT-400 helium-reservoir cryostat. A 1.55-eV, 120-fs,  $p$ -polarised pump pulse with a fluence of 100  $\mu\text{J}/\text{cm}^2$  was used to drive the samples out of equilibrium. A time-delayed 1.31-eV, 120-fs, probe pulse with a fluence of around 30  $\mu\text{J}/\text{cm}^2$  was used to examine the pump-induced reflectivity change  $\Delta R$  of the samples. For the probe pulse we used  $s$  polarisation in order to exclude unwanted interference effects between pump and probe pulses. The diameter of the pump beam exceeded that of the probe beam by a factor of 2.6. The intensity of the reflected probe beam was measured with a silicon photodiode and a lock-in amplifier.

**Theoretical modeling:** We use the Lindblad formalism<sup>41</sup> to derive the dynamical equations for the numbers of bright (spin-0) and dark (spin-1) excitons as well as for the  $z$ -component of the Eu  $4f$  spins from the microscopic Hamiltonian of EuO. Here, acoustic phonons, which assist the bright-dark exciton transformations, comprise a thermal bath at the cryostat temperature  $T$  which induces effective, temperature-dependent spin-flip couplings  $\Gamma^\pm(T)$  between excitons and the Eu  $4f$  magnetic moments, with  $\Gamma^+(T) \ll \Gamma^-(T)$ . In the paramagnetic phase, this leads, after linearisation, to a set of two coupled, dynamical equations for the deviations  $\Delta n_b(t)$ ,  $\Delta n_d(t)$  of the bright or dark exciton densities from their peak values after the pump pulse, respectively,

$$\frac{d}{dt} \begin{pmatrix} \Delta n_b \\ \Delta n_d \end{pmatrix} = \chi(T) \begin{pmatrix} \Delta n_b \\ \Delta n_d \end{pmatrix}, \quad \chi(T) = \begin{pmatrix} \gamma_b & \omega_1 \\ -\omega_2 & \gamma_d \end{pmatrix}. \quad (3)$$

The expressions for  $\gamma_b$ ,  $\gamma_d$ , and  $\omega_1$ ,  $\omega_2$  are derived in the Supplementary Information. The eigenvalues  $\gamma_{1,2}$  of this set of equations are given in Eq. (2), with  $\omega_0^2 = \omega_1\omega_2$ . They depend on temperature through  $\Gamma^\pm(T)$  and change from real- to complex-valued at the critical temperature

$T^*$  of the NHPT, implying the square-root dependence of the complex relaxation parameter  $\gamma''(T) = \text{Im}[\gamma_{1,2}] \propto \sqrt{T - T^*}$ . In the ferromagnetic phase, the temperature-dependent, average magnetisation of the lattice of Eu  $4f$  moments as well as the dynamics of their deviations from the average and the spin-dependent dynamics of the polarised excitons have to be taken into account, leading to a set of four dynamical equations, see Supplementary Information. The appearance of the magnetisation with a critical exponent  $\alpha \approx 1/2$ <sup>18,23</sup> leads to the cusp feature in the relaxation times at the Curie temperature  $T_C$  seen in Fig. 4a which also appears in the experimental data, Fig. 2a.

## AUTHOR CONTRIBUTIONS

J. L. performed the experiments after initial reflectivity studies done by M. M. J. L. and M. T. analyzed the data. K. K. and C. K. produced and characterized the samples. S. P. and M. F. conceived and supervised the experiments. M. T. and J. K. developed the theory. All authors contributed to the discussion and interpretation of the experiment and to the completion of the manuscript.

## COMPETING INTERESTS

The authors declare that they have no competing financial interests.

## CORRESPONDENCE

Correspondence and requests for materials should be addressed to M.F. (email: manfred.fiebig@mat.ethz.ch) or J.K. (email: jkroha@uni-bonn.de).

## ACKNOWLEDGEMENTS

We thank Nazia Kaya and Isabel Reiser for their support in the growth and characterisation of the EuO crystals. This work was financially supported by the Swiss National Science Foundation through SNSF grants No. 200021\_178825, 200021\_219807, 200021\_215423 (J. L., M. F.), by the Deutsche Forschungsgemeinschaft (DFG) through the CRC/TR 185 (277625399) and the Cluster of Excellence ML4Q (EXC 2004/1-390534769) (M. T., J. K.), and through the CRC/TRR 288 (422213477, project A03) (C.K., K. K.), and by JSPS KAKENHI (Grants Nos. 24H00413 and 24H01639) and JST PRESTO (Grant No. JPMJPR23H9) (M. M.), and by DAE through the project Basic Research in Physical and Multidisciplinary Sciences via RIN4001, and the startup support from DAE through NISER and SERB through SERB SRG via Project No. SRG/2022/000290 (S. P.).

- \* manfred.fiebig@mat.ethz.ch  
† jkroha@uni-bonn.de
- <sup>1</sup> E. Beaurepaire, J.-C. Merle, A. Daunois, J.-Y. Bigot. Ultrafast spin dynamics in ferromagnetic nickel. *Phys. Rev. Lett.* **76**, 4250 (1996).
  - <sup>2</sup> D. Fausti, R. I. Tobey, N. Dean, S. Kaiser, A. Dienst, M. C. Hoffmann, S. Pyon, T. Takayama, H. Takagi, and A. Cavalleri. Light-induced superconductivity in a stripe-ordered cuprate. *Science* **331**, 189 (2011).
  - <sup>3</sup> T. Nova, A. Disa, M. Fechner, and A. Cavalleri. Metastable ferroelectricity in optically strained SrTiO<sub>3</sub>. *Science* **364**, 1075 (2019).
  - <sup>4</sup> E. J. Sie, C. M. Nyby, C. D. Pemmaraju, S. J. Park, X. Shen, J. Yang, M. C. Hoffmann, B. K. Ofori-Okai, R. Li, A. H. Reid, S. Weathersby, E. Mannebach, N. Finney, D. Rhodes, D. Chenet, A. Antony, L. Balicas, J. Hone, T. P. Devereaux, T. F. Heinz, X. Wang, and A. M. Lindenberg. An ultrafast symmetry switch in a Weyl semimetal. *Nature* **565**, 61 (2019).
  - <sup>5</sup> A Kirilyuk, AV Kimel, T Rasing. Ultrafast optical manipulation of magnetic order. *Rev. Mod. Phys.* **82**, 2731 (2010).
  - <sup>6</sup> C. Wetli, S. Pal, J. Kroha, K. Kliemt, C. Krellner, O. Stockert, H. v. Löhneysen, M. Fiebig, Time-resolved collapse and revival of the Kondo state near a quantum phase transition. *Nat. Phys.* **14**, 1103 (2018).
  - <sup>7</sup> S. Pal, C. Wetli, F. Zamani, O. Stockert, H. v. Löhneysen, M. Fiebig, J. Kroha. Fermi volume evolution and crystal-field excitations in heavy-fermion compounds probed by time-domain terahertz spectroscopy. *Phys. Rev. Lett.* **122**, 096401 (2019).
  - <sup>8</sup> C. J. Yang, K. Kliemt, C. Krellner, J. Kroha, M. Fiebig, S. Pal. Critical slowing down near a magnetic quantum phase transition with fermionic breakdown. *Nat. Phys.* **19**, 1605 (2023).
  - <sup>9</sup> C.-J. Yang, J. Li, M. Fiebig, and S. Pal. Terahertz control of many-body dynamics in quantum materials. *Nat. Rev. Mater.* **8**, 518 (2023).
  - <sup>10</sup> Y. Ashida, Z. Gong, and Masahito Ueda. Non-Hermitian physics. *Adv. Phys.* **69**, 249 (2020).
  - <sup>11</sup> W. D. Heiss. The physics of exceptional points. *J. Phys. A: Math. Theor.* **45**, 444016 (2012).
  - <sup>12</sup> Y. Wu, W. Liu, J. Geng, X. Song, X. Ye, C.-K. Duan, X. Rong, J. Du. Observation of parity-time symmetry breaking in a single-spin system. *Science* **364**, 878 (2019).
  - <sup>13</sup> A. Li, H. Wei, M. Cotrufo, W. Chen, S. Mann, X. Ni, B. Xu, J. Chen, J. Wang, S. Fan, C.-W. Qiu, A. Alù, L. Chen. Exceptional points and non-Hermitian photonics at the nanoscale. *Nat. Nanotechnol.* **18**, 706 (2023).
  - <sup>14</sup> L. Pan, S. Chen, X. Cui. High-order exceptional points in ultracold Bose gases. *Phys. Rev. A* **99**, 011601(R) (2019).
  - <sup>15</sup> C. Wang, N. Li, J. Xie, C. Ding, Z. Ji, L. Xiao, S. Jia, B. Yan, Y. Hu, Y. Zhao. Exceptional nexus in Bose-Einstein condensates with collective dissipation. *Phys. Rev. Lett.* **132**, 253401 (2024).
  - <sup>16</sup> F. E. Öztürk, T. Lappe, G. Hellmann, J. Schmitt, J. Klaers, F. Vewinger, J. Kroha, and M. Weitz. Observation of a non-Hermitian phase transition in an optical quantum gas. *Science* **372**, 88 (2021).
  - <sup>17</sup> A. Mauger. Indirect Exchange in Europium Chalcogenides. *Phys. Stat. Sol. (b)* **84**, 761 (1977).
  - <sup>18</sup> T. Mairoser, A. Schmehl, A. Melville, T. Heeg, Canella, P. Böni, W. Zander, J. Schubert, D. E. Shai, E. J. Monkman, K. M. Shen, D. G. Schlom, J. Mannhart. Is there an intrinsic limit to the charge-carrier-induced increase of the Curie temperature of EuO? *Phys. Rev. Lett.* **105**, 257206 (2010).
  - <sup>19</sup> T. Stollenwerk and J. Kroha. Theory of Curie temperature enhancement in electron-doped EuO. *Phys. Rev. B* **92**, 205119 (2015).
  - <sup>20</sup> J. M. D. Coey. *Magnetism and Magnetic Materials*. Cambridge University Press (2010).
  - <sup>21</sup> M. Matsubara, A. Schroer, A. Schmehl, A. Melville, C. Becher, M. Trujillo-Martinez, D. G. Schlom, J. Mannhart, J. Kroha, and M. Fiebig. Ultrafast optical tuning of ferromagnetism via the carrier density. *Nat. Commun.* **6**, 6724 (2015).
  - <sup>22</sup> P. G. Steeneken, L. H. Tjeng, I. Elfimov, G. A. Sawatzky, G. Ghiringhelli, N. B. Brookes, and D.-J. Huang. Exchange splitting and charge carrier spin polarization in EuO. *Phys. Rev. Lett.* **88**, 047201 (2002).
  - <sup>23</sup> M. Arnold and J. Kroha. Simultaneous ferromagnetic metal-semiconductor transition in electron-doped EuO. *Phys. Rev. Lett.* **100**, 046404 (2008).
  - <sup>24</sup> J. Feinleib, W. J. Scouler, J. O. Dimmock, J. Hanus, T. B. Reed, and C. R. Pidgeon. Spin-polarized splittings in the temperature-dependent reflectance of EuO. *Phys. Rev. Lett.* **22**, 1385 (1969).
  - <sup>25</sup> H.Y. Wang, J. Schoenes, and E. Kaldis. Magneto-optical polar Kerr effect of EuO. *Helv. Phys. Acta* **59**, 102 (1986).
  - <sup>26</sup> F. Liu, T. Makino, T. Yamasaki, K. Ueno, A. Tsukazaki, T. Fukumura, Y. Kong, and M. Kawasaki. Ultrafast time-resolved Faraday rotation in EuO thin films. *Phys. Rev. Lett.* **108**, 257401 (2012).
  - <sup>27</sup> T. B. Reed, and R. E. Fahey. Growth of EuO, EuS, EuSe and EuTe single crystals. *J. Cryst. Growth* **8**, 337 (1971).
  - <sup>28</sup> F. Sun, Q. Wu, Y. L. Wu, H. Zhao, C. J. Yi, Y. C. Tian, H. W. Liu, Y. G. Shi, H. Ding, X. Dai, P. Richard, and J. Zhao. Coherent helix vacancy phonon and its ultrafast dynamics waning in topological Dirac semimetal Cd<sub>3</sub>As<sub>2</sub>. *Phys. Rev. B* **95**, 235108 (2017).
  - <sup>29</sup> V. Goian, R. Held, E. Bousquet, Y. Yuan, A. Melville, H. Zhou, V. Gopalan, P. Ghosez, N. A. Spaldin, D. G. Schlom, and S. Kamba. Making EuO multiferroic by epitaxial strain engineering. *Commun. Mater.* **1**, 74 (2020).
  - <sup>30</sup> D. B. But, M. Mittendorff, C. Consejo, F. Teppe, N. N. Mikhailov, S. A. Dvoretiskii, C. Faugeras, S. Winnerl, M. Helm, W. Knap, M. Potemski, and M. Orlita. Suppressed Auger scattering and tunable light emission of Landau-quantized massless Kane electrons. *Nat. Photonics* **13**, 783 (2019).
  - <sup>31</sup> A. S. Sharma, S. J. Sreerag, and R. N. Kini. Temperature-dependent ultrafast hot carrier dynamics in the dilute bismide alloy GaSb<sub>1-x</sub>Bi<sub>x</sub> ( $x \lesssim 0.4\%$ ). *J. Appl. Phys.* **135**, 035701 (2024).
  - <sup>32</sup> J. Ye, T. Yan, B. Niu, Y. Li, and X. Zhang. Nonlinear dynamics of trions under strong optical excitation in monolayer MoSe<sub>2</sub>. *Sci. Rep.* **8**, 2389 (2018).
  - <sup>33</sup> A. J. Sabbah, and D. M. Riffe. Femtosecond pump-probe reflectivity study of silicon carrier dynamics. *Phys. Rev. B* **66**, 165217 (2002).
  - <sup>34</sup> S. S. Prabhu, and A. S. Vengurlekar. Dynamics of the pump-probe reflectivity spectra in GaAs and GaN. *J. Appl. Phys.* **95**, 7803 (2004).



- <sup>35</sup> A. Di Cicco, F. D'Amico, G. Zgrablic, E. Principi, R. Gunnella, F. Bencivenga, C. Svetina, C. Masciovecchio, F. Parmigiani, and A. Filipponi. Probing phase transitions under extreme conditions by ultrafast techniques: Advances at the Fermi@Elettra free-electron-laser facility. *J. Non-Cryst. Solids* **357**, 2641 (2011).
- <sup>36</sup> A. Di Cicco, G. Polzoni, R. Gunnella, A. Trapananti, M. Minicucci, S. J. Rezvani, D. Catone, L. Di Mario, J. S. Pelli Cresi, S. Turchini, and F. Martelli. Broadband optical ultrafast reflectivity of Si, Ge and GaAs. *Sci. Rep.* **10**, 17363 (2020).
- <sup>37</sup> A. J. Sabbah, and D. M. Riffe. Measurement of silicon surface recombination velocity using ultrafast pump-probe reflectivity in the near infrared. *J. Appl. Phys.* **88**, 6954 (2000).
- <sup>38</sup> V. Unikandanunni, F. Rigoni, M. C. Hoffmann, P. Vavassori, S. Urazhdin, and S. Bonetti. Ultrafast electron dynamics in platinum and gold thin films driven by optical and terahertz fields. *Appl. Phys. Lett.* **120**, 021601 (2022).
- <sup>39</sup> I. Madan, T. Kurosawa, Y. Toda, M. Oda, T. Mertelj, P. Kusar, and D. Mihailovic. Separating pairing from quantum phase coherence dynamics above the superconducting transition by femtosecond spectroscopy. *Sci. Rep.* **4**, 5656 (2014).
- <sup>40</sup> T. Mitani and T. Koda, Wannier excitons in the ferromagnetic semiconductors EuO and EuS, *Phys. Rev. B* **12**, 2311 (1975).
- <sup>41</sup> H.-P. Breuer and F. Petriccione. *The theory of open quantum systems*. Oxford University Press (2010).
- <sup>42</sup> C.P. Zelle, R. Daviet, A. Rosch, and S. Diehl. Universal Phenomenology at Critical Exceptional Points of Nonequilibrium  $O(N)$  Models. *Phys. Rev. X* **14**, 021052 (2024).
- <sup>43</sup> K. Ahn, A. O. Pecharsky, K. A. Gschneidner, Jr., and V. K. Pecharsky. Preparation, heat capacity, magnetic properties, and the magnetocaloric effect of EuO. *J. Appl. Phys.* **97**, 063901 (2005).

# Supplementary Information: Discovery of a non-Hermitian phase transition in a bulk condensed-matter system

Jingwen Li,<sup>1</sup> Michael Turaev,<sup>2</sup> Masakazu Matsubara,<sup>3,4,5</sup> Kristin Kliemt,<sup>6</sup>  
Cornelius Krellner,<sup>6</sup> Shovon Pal,<sup>7</sup> Manfred Fiebig,<sup>1,\*</sup> and Johann Kroha<sup>2,8,†</sup>

<sup>1</sup>*Department of Materials, ETH Zurich, Vladimir-Prelog-Weg 4, 8093 Zurich, Switzerland*

<sup>2</sup>*Physikalisches Institut and Bethe Center for Theoretical Physics, University of Bonn, 53115 Bonn, Germany*

<sup>3</sup>*Department of Physics, Tohoku University, Sendai 980-8578, Japan*

<sup>4</sup>*Center for Science and Innovation in Spintronics, Tohoku University, Sendai 980-8577, Japan*

<sup>5</sup>*PRESTO, Japan Science and Technology Agency (JST), Kawaguchi 332-0012, Japan*

<sup>6</sup>*Physikalisches Institut, Goethe-Universität Frankfurt, 60438 Frankfurt, Germany*

<sup>7</sup>*School of Physical Sciences, National Institute of Science Education and Research, An OCC of HBNI, Jatni, 752 050 Odisha, India*

<sup>8</sup>*School of Physics and Astronomy, University of St. Andrews,  
North Haugh, St. Andrews, KY16 9SS, United Kingdom*

## Sample quality and characterization

We determine the sample composition via energy dispersive X-ray spectroscopy (EDX), the crystal structure by powder X-ray diffraction (PXRD), and the orientation of the as-grown EuO using a Laue device, Müller Micro 91, with a tungsten anode. The typical Laue pattern (Fig. S1a) shows sharp reflexes indicating a high crystallinity of the samples. Furthermore, the simulation of the pattern yields [100] cleavage planes of the crystals. By indexing the peaks using the software “OrientExpress”, we confirm the rock-salt crystal structure and the lattice parameter ( $a = 5.1378$  Å), which agrees with the literature value of EuO single crystals<sup>1-3</sup>.

We further checked the magnetic properties by examining the magnetic susceptibility between 1.8 K and 300 K at  $\mu_0 H = 0.01$  T using a Quantum Design Physical Property Measurement System (PPMS). The sample was cooled in zero field prior to each measurement. The inset of Fig. S1b shows the magnetic susceptibility  $\chi_{\text{mol}}$  of EuO in the whole measured temperature range. The susceptibility  $\chi_{\text{mol}}$  exhibits an abrupt change at  $T_C = 69$  K at the transition into the magnetically ordered state, agreeing with a typical values for transitions between a ferromagnetic and a paramagnetic phase. The linear temperature dependence of  $\chi_{\text{mol}}^{-1}$  in the paramagnetic phase indicates Curie-Weiss behavior. We determine the transition temperature by extrapolation of the linear fit as  $T_C \approx 69$  K, which agrees precisely with the literature value<sup>4,5</sup>. This implies an undetectably low charge-defect density in our EuO samples, since  $T_C$  would sensitively shift to higher values even upon small amounts of carrier doping  $< 0.1$  %<sup>5,6</sup>. This confirms that the conduction band is empty before the pump excitation. The near-constant value below  $T_C$  indicates a negligible coercivity in the susceptibility measurements, again in agreement with the literature<sup>1</sup>. The absence of a low-temperature increase of  $\chi_{\text{mol}}$  below 10 K<sup>1</sup> confirms the absence of compositions like Eu<sub>3</sub>O<sub>4</sub>, which would order antiferromagnetically at around 5 K.

The ferromagnetic phase transition is also confirmed by the heat-capacity measurement between 1.8 K and 200 K in zero field using the PPMS, as displayed in Fig. S1c. The pronounced  $\lambda$ -like peak centered at 69 K matches the

second-order transition from the ferromagnetic to the paramagnetic phase.

## Fit of experimental data

To quantitatively investigate the evolution of the relaxation dynamics, we fit the temperature dependence of  $\Delta R/R$  according to the relation

$$y = C_1 \cdot e^{-\gamma_1 t} + C_2 \cdot e^{-\gamma_2 t} + y_0. \quad (\text{S1})$$

Depending on the temperature range in question, we may choose the relaxation rates  $\gamma_{1,2}$  as real or complex, the amplitudes  $C_{1,2}$  as positive, negative, or complex, and the offset  $y_0$  as non-zero or zero, as discussed in the following.

At low temperature, the time dependence of  $\Delta R/R$  in the main text suggests a bi-exponential relaxation, and we choose  $C_{1,2} > 0$  and  $\gamma_{1,2}$  as real, so that the latter represent relaxation rates with  $\tau_{\text{slow}} = 1/\gamma_1$ ,  $\tau_{\text{fast}} = 1/\gamma_2$  as the associated relaxation times. The offset  $y_0 > 0$  describes the reflectivity change associated with the long-lasting insulator-metal transition resulting from the Stoner band splitting in the ferromagnetic phase; see the main text. Typical fit results are presented in Fig. S2a, **b**. They show that the bi-exponential model perfectly describes the relaxation behavior of  $\Delta R/R$  at low temperature (panel **a**) but fails to reproduce the behaviour of the reflectivity at high temperature (panel **b**), where  $\Delta R/R$  exhibits a negative regime.

Negative contributions to the reflectivity change might, for instance, arise from radiationless Auger recombination. Even though we excluded this process in the main text for reasons of principle, we nevertheless attempted to fit it by choosing  $C_1 < 0$  and keeping  $C_2 > 0$  and  $\gamma_{1,2}$  real as before. The results are displayed in Fig. S3. Even though a good agreement with the experimental results is achieved at selected temperatures, see Fig. S3a, the temperature dependence of the set of fits in Fig. S3b exhibits an unphysical, erratic behavior for the relaxation time  $\tau_{\text{slow}}$ . Note that the discontinuous trend between 100 and 200 K is also expressed by the enormous error bars of the associated fit values; see the caption of Fig. S3. Hence, the negative-

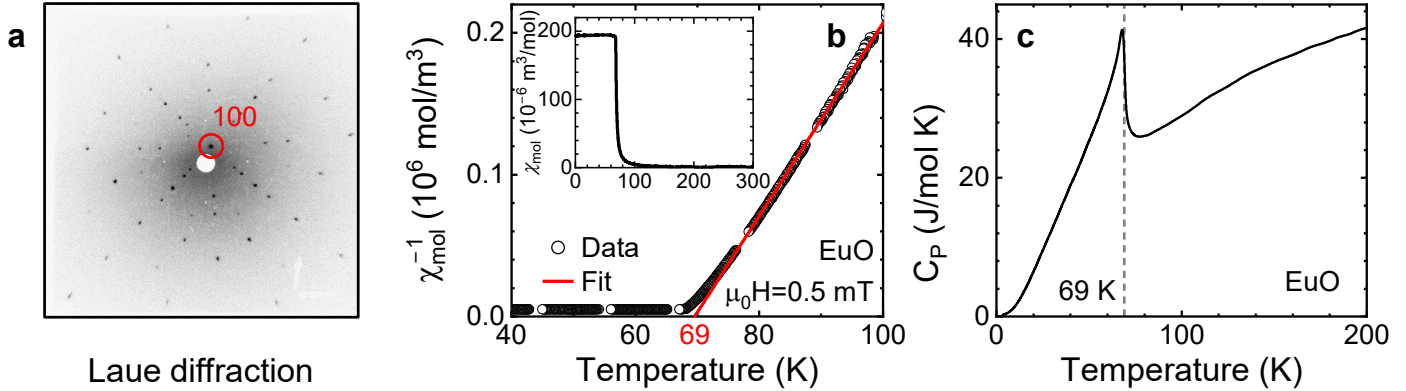


Figure S1. Characterisation of our EuO bulk single crystals. **a**, The Laue pattern of the crystallographic [100] direction shows the four-fold symmetry of the cubic lattice. **b**, Inverse magnetic susceptibility of EuO measured in a 0.5 mT magnetic field. The extrapolation of the linear fit leads to  $T_C \approx 69$  K. The inset shows the magnetic susceptibility from 1.8 K to room temperature. **c**, Zero-field specific heat.

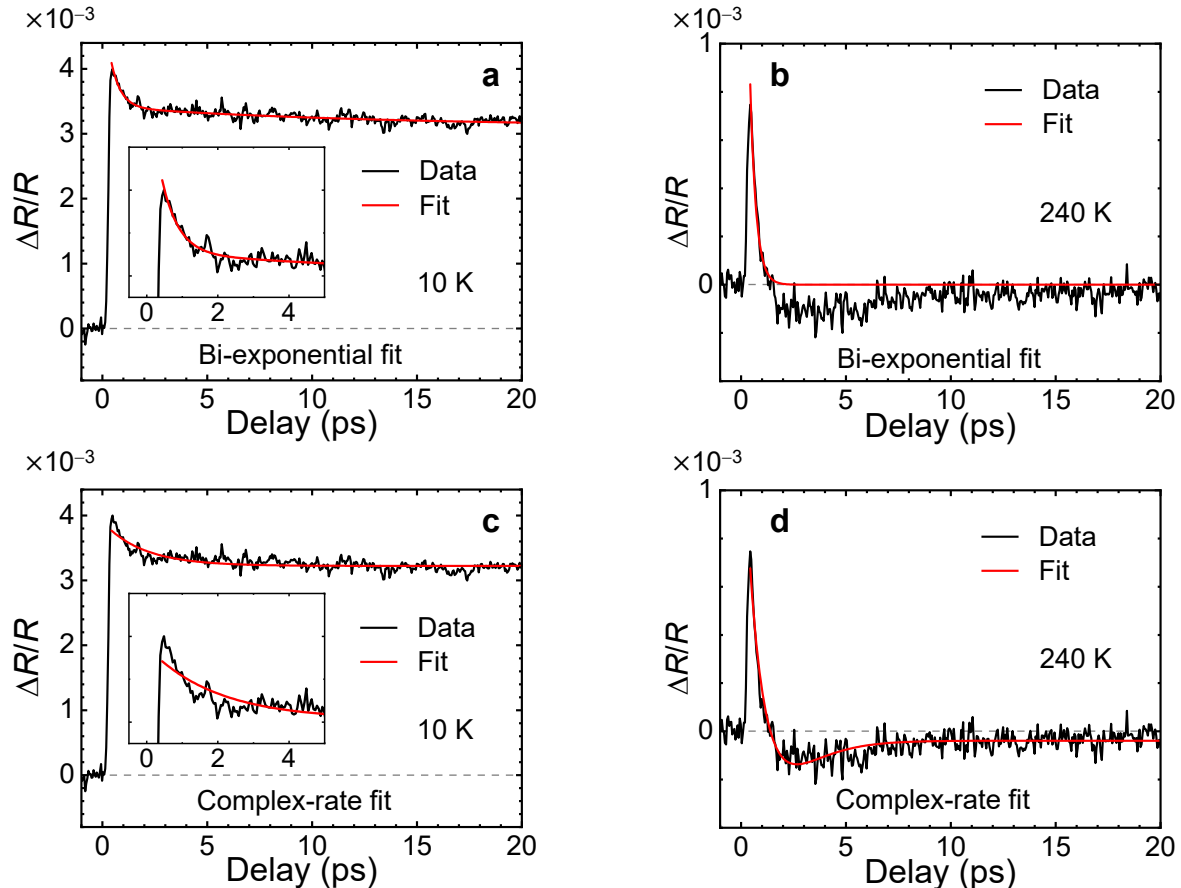


Figure S2. Normalised, pump-induced reflectivity  $\Delta R/R$  data and fit results of Eq. (S1) for the bi-exponential and the complex-rate scenarios discussed in the supplementary text. **a**, **b**, bi-exponential fit with real and positive values  $C_{1,2}$ ,  $\gamma_{1,2}$ , and  $y_0$ . It reproduces the low-temperature data well, but fails to reproduce the negative part of  $\Delta R/R$  at high temperature. **c**, **d**, Data and fit results with complex values  $C_{1,2} = C_0 e^{\pm i\varphi_0}$ ,  $\gamma_{1,2} = \gamma' \pm i\gamma''$ , and  $y_0 = 0$ . This model describes the data appropriately at high temperature, but fails at low temperature, indicating a qualitative change of the dynamics at an intermediate temperature  $T^*$ . The insets in **a** and **c** are zoomed-in views for better visualisation of the fit quality.

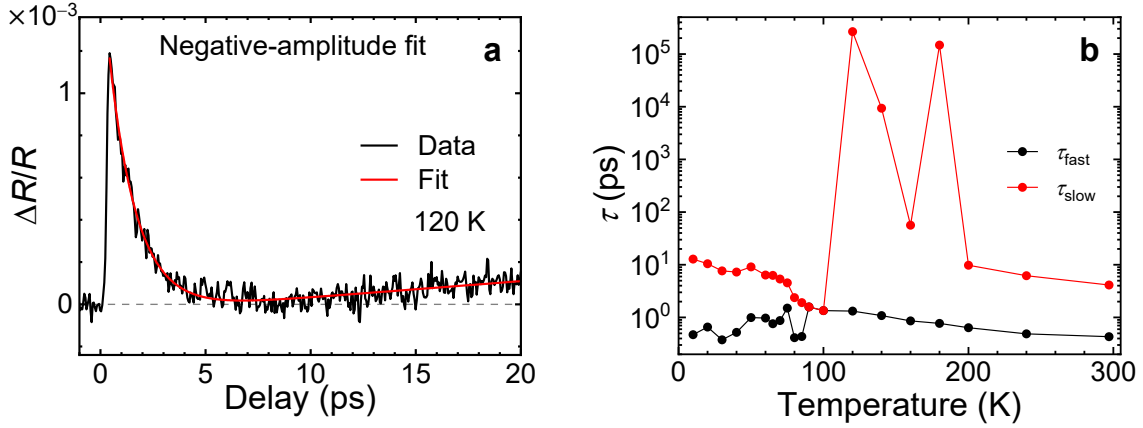


Figure S3. Normalised, pump-induced reflectivity data  $\Delta R/R$  and fit result with the negative-amplitude model (both positive and negative coefficients  $C_1, C_2$  allowed). **a**, Time trace and fit at 120 K. **b**, Relaxation times  $\tau_{\text{slow}}, \tau_{\text{fast}}$  extracted from fitting the negative-amplitude model. Although individual time traces can be fitted well, the erratic temperature dependence of the extracted relaxation time  $\tau_{\text{fast}}$  and the associated huge fit errors of  $\sigma_\tau \approx 4.4 \times 10^6$  ps demonstrate the infeasibility of the fit.

amplitude model ( $C_1 < 0$ ) and any physical processes associated with it must be discarded.

Instead we emulate the region with  $\Delta R/R < 0$  by assuming complex values for  $C_{1,2}$  and  $\gamma_{1,2}$ . Specifically, we set  $C_{1,2} = C_0 e^{\pm i\varphi_0}$  and  $\gamma_{1,2} = \gamma' \pm i\gamma''$ , which ensures that the resulting observable  $\Delta R/R < 0$  in Eq. (S1) is still a real value. We furthermore set  $y_0 = 0$  because there are no insulator-metal transition and Stoner splitting in the high-temperature paramagnetic regime. This leads to two adjustable parameters only,  $\gamma'$  and  $\gamma''$ , since the amplitude  $C_0$  is absorbed in the normalisation of the experimental signal and the phase  $\varphi_0$  is trivially fixed by the position of the zero-crossing of the experimentally observed time traces (see, e.g. Fig. S2d). From Fig. S2c, d we see that the complex-rate model fits the experimental data very well at high temperature, but, as expected, fails at low temperature.

To quantify the feasibility of the bi-exponential and complex-rate fits and evaluate the transition temperature  $T^*$  between the respective regimes, we assess the fit quality by the parameter

$$\mathfrak{R}^2 = 1 - \frac{\sum_i (y_i - f_i)^2}{\sum_i (y_i - \bar{y})^2}, \quad (\text{S2})$$

where  $y_i$  represent the measured data at the observation times  $t_i$ ,  $f_i$  is the value predicted by the fitting model, and  $\bar{y}$  is the average of the measured data. Thus, the larger  $\mathfrak{R}^2$ , the better the model describes the experimental data. Figure S4 shows the difference  $\mathfrak{R}_{\text{real}}^2 - \mathfrak{R}_{\text{complex}}^2$  between the real- and complex-valued relaxation models. We see that the bi-exponential model with positive amplitudes is appropriate at low temperature, whereas the complex-rate model consistently describes the data at high temperature. This behaviour is characteristic for a NHPT, as discussed in detail in the main text. The transition temperature of the NHPT, where the change from real to complex relaxation occurs, is derived as  $T^* = (84 \pm 5)$  K from the temperature dependence of  $\gamma''$  in the main text. This value is in per-

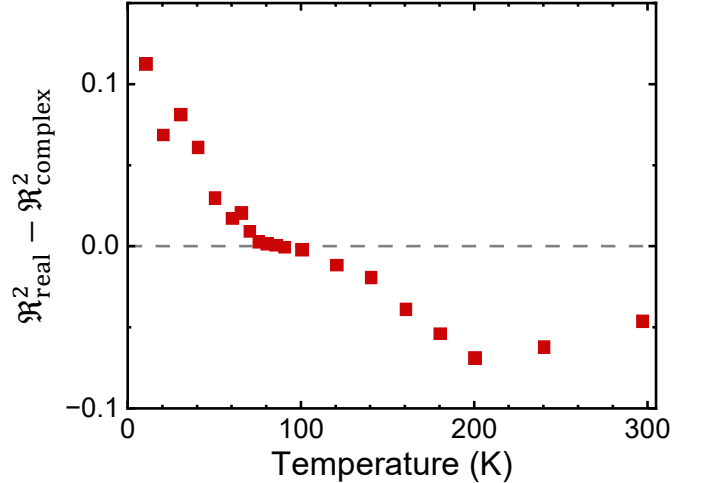


Figure S4. Difference in fit quality according to Eq. (S2) between the bi-exponential and complex-rate scenarios. Better suitability of the former or latter are indicated by positive or negative values of  $\mathfrak{R}_{\text{real}}^2 - \mathfrak{R}_{\text{complex}}^2$ , respectively. We see that with increasing temperature, a transition from bi-exponential to complex-rate behaviour occurs with the zero crossing at 85 K in excellent agreement with the results in the main text.

fect agreement with the zero-crossing of  $\mathfrak{R}_{\text{real}}^2 - \mathfrak{R}_{\text{complex}}^2$  at  $T^* = 85$  K in Fig. S4.

### Theory of exciton dynamics

The dynamical variables of the photoexcited EuO system are the density of bright (spin-0) and dark (spin-1) excitons, represented by bosonic creation and destruction operators  $a_0^\dagger, a_0$  and  $a_{\pm 1}^\dagger, a_{\pm 1}$  respectively, as well as the orientation  $S_{i,z}$  of the Eu  $4f$  magnetic moments  $\vec{S}_i$  on lattice site  $i$ ,  $S_{i,z} = \pm 1/2, \pm 3/2, \dots, \pm S$ ,  $S = 7/2$ . The

effective Hamiltonian for these excitations reads,

$$H_{\text{ex}} = \sum_{m=\pm 1} \hbar\Omega_m a_m^\dagger a_m - J \sum_{\langle i,j \rangle} \vec{S}_i \cdot \vec{S}_j + \sum_k \varepsilon_k b_k^\dagger b_k + J_{df} \sum_{m=\pm, k} (b_k + b_k^\dagger) \left[ a_m^\dagger a_0 S^{-m} + a_0^\dagger a_m S^m \right], \quad (\text{S3})$$

where  $\hbar\Omega_m > 0$  is the excitation energy of a dark exciton ( $m = \pm 1$ ) with respect to a bright exciton,  $J$  is the ferromagnetic-polaron exchange coupling between the Eu  $4f$  moments on a Heisenberg lattice, and the last term describes the transfer between bright and dark excitons. It is induced by the spin-exchange coupling  $J_{df}$  between the electron spin in a  $5d(t_{2g})$  orbital as a constituent of an exciton and the  $4f$  moments on neighboring Eu sites<sup>7</sup>. Here and in the following,  $S^\pm$  represent the corresponding  $4f$ -spin raising and lowering operators, respectively, and we suppress the index of neighboring Eu lattice sites for simplicity of notation. Note that the triplet dark-exciton state

with  $m = 0$  is not accessed by the spin-flip processes. The bright-dark exciton transitions are assisted by absorption or emission of phonons with dispersion  $\varepsilon_k$ , described by phonon creation and destruction operators  $b_k^\dagger$ . The phonon system comprises a thermal, Markovian bath at the cryostat temperature  $T$  which we treat by the Lindblad formalism. This leads, after lengthy, but straight-forward operator algebra<sup>8,9</sup> to the Lindblad master equation for the density matrix  $\hat{\rho}(t)$  of the coupled exciton-Eu  $4f$ -moment system,

$$\begin{aligned} \frac{d\hat{\rho}(t)}{dt} = & i[\hat{\rho}(t), H_0] + p(t) L[a_0^\dagger] \hat{\rho}(t) + R L[a_0] \hat{\rho}(t) \\ & + \sum_{m=\pm 1} \left\{ \Gamma^+ L[a_m^\dagger a_0 S^{-m}] \hat{\rho}(t) + \Gamma^- L[a_0^\dagger a_m S^m] \hat{\rho}(t) \right\}. \end{aligned} \quad (\text{S4})$$

Here, the Lindblad superoperator  $L$  of an operator  $A$  acting on the density matrix is defined as

$$L[A] \hat{\rho} = A\hat{\rho}A^\dagger - (A^\dagger A\hat{\rho} + \hat{\rho}A^\dagger A)/2. \quad (\text{S5})$$

The terms on the right-hand side of Eq. (S4) thus describe, in the order of appearance, the coherent von-Neumann time evolution, the excitation of bright excitons by the external laser pulse  $p(t)$ , the radiative decay of bright excitons with amplitude  $R$ , and the phonon-assisted bright-dark and dark-bright exciton transformations mediated by lowering and raising the Eu  $4f$  spin, respectively. For reasons of energy conservation (rotating wave approximation<sup>10</sup>), the former process is accompanied by phonon absorption, the latter by phonon emission, since  $\Omega_{\pm 1} > 0$ . The bare system Hamiltonian  $H_0$  consists of the first two terms of Eq. (S3) and the bright-dark/dark-bright exciton transformation terms without coupling to phonons. Eq. (S4) contains the time-dependent, pulsed pump rate  $p(t)$  whose temporal integral represents the pump fluence  $P$ . Integrating out the thermal phonon bath from the Hamiltonian  $H_{\text{ex}}$  leads to the effective, temperature-dependent couplings for dark-exciton excitation and de-excitation processes in the

master Eq. (S4), respectively,

$$\Gamma_m^+(T) = \frac{J_{df}^2}{2} N_{\text{ph}}(\Omega_m) B(\Omega_m) \quad (\text{S6})$$

$$\Gamma_m^-(T) = \frac{J_{df}^2}{2} N_{\text{ph}}(\Omega_m) [1 + B(\Omega_m)], \quad (\text{S7})$$

where  $B(\Omega_m) = 1/[\exp(\hbar\Omega_m/k_B T) - 1]$  is the Bose-Einstein distribution function at temperature  $T$ , with  $k_B$  the Boltzmann and  $\hbar$  the reduced Planck constant, and  $N_{\text{ph}}(\Omega_m)$  the phonon spectral density per unit cell at the dark-exciton excitation energy  $\hbar\Omega_m$ ,  $m = \pm 1$ . The excitation and de-excitation amplitudes thus obey the detailed-balance or Kennard-Stepanov relation,  $\Gamma_m^+/\Gamma_m^- = \exp(-\hbar\Omega_m/k_B T)$ . At the relevant temperatures we have in general,  $\Gamma_m^+ \ll \Gamma_m^-$ .

The statistical expectation value of a physical quantity  $\hat{X}$  is defined as  $\langle \hat{X} \rangle := \text{tr} \left\{ \hat{\rho}(t) \hat{X} \right\}$ . We use the short-hand notation  $n_m = \langle a_m^\dagger a_m \rangle$  for the expectation values of the exciton density operators,  $m = 0, \pm 1$ , and  $S_z = \langle \hat{S}_z \rangle$  for the expectation value of the  $z$  component of the  $4f$  spin. Inserting Eqs. (S4) and (S5), we thus obtain the non-linear rate equations for the dynamics following the initial pump pulse,

$$\begin{aligned} \frac{dn_0}{dt} = & -Rn_0 - \Gamma_1^+ \langle S^+ S^- \rangle (1+n_1)n_0 - \Gamma_{-1}^+ \langle S^- S^+ \rangle (1+n_{-1})n_0 \\ & + \Gamma_1^- \langle S^- S^+ \rangle (1+n_0)n_1 + \Gamma_{-1}^- \langle S^+ S^- \rangle (1+n_0)n_{-1} \end{aligned} \quad (\text{S8})$$

$$\frac{dn_1}{dt} = -\Gamma_1^- \langle S^- S^+ \rangle (1+n_0)n_1 + \Gamma_1^+ \langle S^+ S^- \rangle (1+n_1)n_0 \quad (\text{S9})$$

$$\frac{dn_{-1}}{dt} = -\Gamma_{-1}^- \langle S^+ S^- \rangle (1+n_0)n_{-1} + \Gamma_{-1}^+ \langle S^- S^+ \rangle (1+n_{-1})n_0 \quad (\text{S10})$$

$$\begin{aligned} \frac{dS_z}{dt} = & -\Gamma_1^+ \langle S^+ S^- \rangle (1+n_1)n_0 + \Gamma_{-1}^+ \langle S^- S^+ \rangle (1+n_{-1})n_0 \\ & - \Gamma_{-1}^- \langle S^+ S^- \rangle (1+n_0)n_{-1} + \Gamma_1^- \langle S^- S^+ \rangle (1+n_0)n_1, \end{aligned} \quad (\text{S11})$$

where  $\langle S^\pm S^\mp \rangle = S(S+1) - \langle \hat{S}_z^2 \rangle \pm \langle \hat{S}_z \rangle$ . Note that the coherent time evolution due to  $H_0$  does not contribute because the bright-dark exciton conversion without phonon assistance is effectively forbidden by energy conservation ( $\Omega_{\pm 1} > 0$ ) and the commutator involving the number operators contained in  $H_0$  vanishes under the trace. The dynamical equations (S8)-(S11) may be simplified by defining the total density of dark excitons as  $n_d = n_1 + n_{-1}$  and their spin polarisation as  $m_d = n_1 - n_{-1}$  and observing that the total magnetisation, comprised of the spin polarisations of the  $4f$  moments and of the dark excitons, is conserved by these dynamics, that is,  $dm_d/dt = -dS_z/dt$ .

In order to analyze the relaxation behavior of the system, the rate equations (S8)-(S11) are expanded to linear order in the dynamical variables about their peak values,

$\bar{n}_m$ ,  $m = 0, \pm 1$ , after the excitation by the initial pump-laser pulse. This leads to a set of four coupled, linear rate equations for the deviations of the exciton densities and of the  $4f$ -spin orientation  $S_z(t)$  from their respective initial values.

In the **paramagnetic phase**, the  $4f$  magnetisation before the pump pulse is  $S_z(0) = 0$ , and for symmetry reasons, the populations of up-spin and down-spin dark excitons are equal,  $n_1 = n_{-1}$ . It then follows from Eq. (S11) that  $S_z(t) = 0$  at all times. Hence, the transverse  $4f$  spin correlator  $C_\perp = \langle S^+ S^- \rangle = \langle S^- S^+ \rangle = S(S+1) - \langle \hat{S}_z^2 \rangle = \text{const.}$  and  $\Gamma_1^\pm = \Gamma_{-1}^\pm \equiv \Gamma^\pm$ . The linearised dynamical equations then simplify to a set of two coupled equations for the bright and dark exciton densities, respectively,

$$\begin{aligned} \frac{d}{dt} \begin{pmatrix} \Delta n_b \\ \Delta n_d \end{pmatrix} &= \chi(T) \begin{pmatrix} \Delta n_b \\ \Delta n_d \end{pmatrix} \\ \chi(T) &= \begin{pmatrix} -R + 2C_\perp [\Gamma^- \bar{n}_d - \Gamma^+(1 + \bar{n}_d)] & 2C_\perp [\Gamma^-(1 + \bar{n}_b) - \Gamma^+ \bar{n}_b] \\ -C_\perp [\Gamma^- \bar{n}_d - \Gamma^+(1 + \bar{n}_d)] & C_\perp [\Gamma^+ \bar{n}_b - \Gamma^-(1 + \bar{n}_b)] \end{pmatrix}, \end{aligned} \quad (\text{S12})$$

where we used the notation for the deviation of the bright and dark exciton densities from their respective initial values,  $\Delta n_b(t) = n_b(t) - \bar{n}_b$  and  $\Delta n_d(t) = n_d(t) - \bar{n}_d$ , and  $\bar{n}_b, \bar{n}_d$  are the corresponding initial values after the pump pulse. The dynamical matrix  $\chi(T)$  has the eigenvalues

$$\gamma_{1,2}(T) = \left[ \gamma_b + \gamma_d \pm \sqrt{(\gamma_b - \gamma_d)^2 - 4\omega_0^2} \right] / 2, \quad (\text{S13})$$

with

$$\begin{aligned} \gamma_b &= -R + 2C_\perp [\Gamma^- \bar{n}_d - \Gamma^+(1 + \bar{n}_d)] \\ \gamma_d &= C_\perp [\Gamma^+ \bar{n}_b - \Gamma^-(1 + \bar{n}_b)] \end{aligned} \quad (\text{S14})$$

$$\omega_0 = C_\perp \sqrt{2 [\Gamma^-(1 + \bar{n}_b) - \Gamma^+ \bar{n}_b] [\Gamma^- \bar{n}_d - \Gamma^+(1 + \bar{n}_d)]}.$$

The eigenvalues depend on temperature through  $\Gamma^-(T)$  and  $\Gamma^+(T)$  [c.f. Eqs. (S6), (S7)] and change from real

$R$	$\bar{n}_b$	$\bar{n}_d$	$\Gamma^-/R$	$\Gamma^+/R$
1 THz	0.07	0.25 $n_b$	$0.06 + 6.9 \times 10^{-4} \cdot k_B T/R$	$\Gamma^-/100$

Table S1. Parameters used in the paramagnetic phase to produce Fig. 4 of the main article and Fig. S5.

to complex at the critical temperature  $T^*$  of the exceptional point (EP). Expanding the argument of the square root in Eq. (S13) to linear order of  $(T - T^*)$ , it follows that the imaginary relaxation parameter behaves as  $\gamma'' = \text{Im}(\gamma_{1,2}) \sim \sqrt{T - T^*}$ , as shown in Fig. 4b of the main text. The parameter values used for the numerical evaluations are shown in Table S1. Fig. S5 shows typical time traces of bright and dark exciton densities in the phases of bi-exponential and the complex relaxation of the NHPT, respectively.

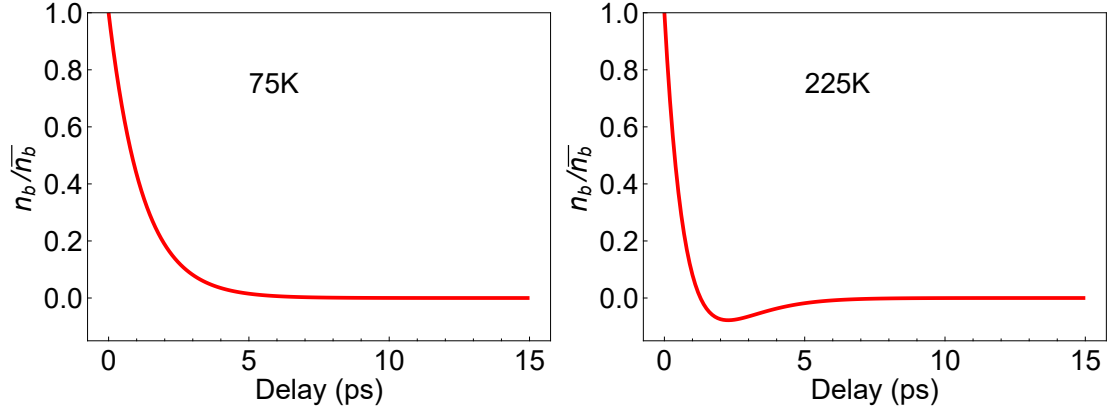


Figure S5. Theoretical time traces of the bright-exciton population  $n_b(t)$ , computed from the dynamical equations (S12) on the bi-exponential side (75 K) and on the complex-rate side (225 K) of the NHPT, respectively. The data are normalised to the initial value  $\bar{n}_b = n_b(0)$ . The parameter values used for the calculation are given in Table S1.

In the **ferromagnetic phase**, the  $4f$  magnetisation acquires a non-vanishing, static value  $M(T)$  in addition to its time-dependent variations,  $\langle S_z \rangle = M + \langle \Delta S_z \rangle$ , and the up-spin and down-spin dark-exciton populations are no longer equal,  $n_1 \neq n_{-1}$ . In this case, the full set of four dynamical equations (S8)–(S11), after linearisation, must be simultaneously solved. According to ferromagnetic

mean-field theory, which is well controlled for the large Eu  $S = 7/2$  spins, the equilibrium magnetisation has a square-root temperature dependence near the Curie temperature,  $M(T) = M_0\sqrt{T_C - T}$ , which leads to the cusp signature in the relaxation times at  $T_C$ , as shown in Fig. 4a of the main text.

\* manfred.fiebig@mat.ethz.ch

† jkroha@uni-bonn.de

<sup>1</sup> K. Ahn, A. O. Pecharsky, K. A. Gschneidner, Jr., and V. K. Pecharsky. Preparation, heat capacity, magnetic properties, and the magnetocaloric effect of EuO. *J. Appl. Phys.* **97**, 063901 (2005).

<sup>2</sup> R. A. Belayev, V. V. Bondarenko, V. P. Vyskubov, S. S. Kiparisov, V. A. Lazarevski, and V. M. Tyugin, *Properties of Europium Oxides*, Tech. report, 2883, Oak Ridge National Laboratory (1974).

<sup>3</sup> J. F. Dillon, Jr. and C. E. Olsen, Ferromagnetic resonance of EuO, *Phys. Rev.* **135**, A434 (1964).

<sup>4</sup> T. R. McGuire and M. W. Shafer, Ferromagnetic Europium Compounds, *J. Appl. Phys.* **35**, 984 (1964).

<sup>5</sup> T. Mairoser, A. Schmehl, A. Melville, T. Heeg, Canella, P. Böni, W. Zander, J. Schubert, D. E. Shai, E. J. Monkman, K. M. Shen, D. G. Schlom, J. Mannhart. Is there an intrinsic

limit to the charge-carrier-induced increase of the Curie temperature of EuO? *Phys. Rev. Lett.* **105**, 257206 (2010).

<sup>6</sup> T. Stollenwerk and J. Kroha. Theory of Curie temperature enhancement in electron-doped EuO. *Phys. Rev. B* **92**, 205119 (2015).

<sup>7</sup> A. Mauger. Indirect Exchange in Europium Chalcogenides. *Phys. Stat. Sol. (b)* **84**, 761 (1977).

<sup>8</sup> H.-P. Breuer and F. Petriccione. *The theory of open quantum systems*. Oxford University Press (Oxford, New York, 2010).

<sup>9</sup> F. E. Öztürk, T. Lappe, G. Hellmann, J. Schmitt, J. Klaers, F. Vewinger, J. Kroha, and M. Weitz. Fluctuation dynamics of an open photon Bose-Einstein condensate. *Phys. Rev. A* **100**, 043803 (2019).

<sup>10</sup> C. C. Gerry. *Introductory quantum optics*. 3rd edition, Cambridge University Press (Cambridge, New York, 2008).